ATLAS NOTE

November 27, 2009

TCAD Simulation of ATLAS Pixel Guard Ring and Edge Structure for Super-LHC Upgrade

Abdenour Lounis[a], Dominique Martinot[b], Giovanni Calderini[b]
Giovanni Marchiori[b], Mathieu Benoit[a], Nicoleta Dinu[a]
On behalf of ATLAS Upgrade Planar Pixel sensor R&D collaboration
[a] LAL, CNRS/IN2P3,University of Paris-Sud, Orsay, France
[b] LPNHE, CNRS/IN2P3, University of Paris VI, Paris, France

ATL-UPGRADE-PUB-2010-001
18 January 2010

Abstract

In this work, the magnitude of the electric field and the depletion inside a simplified two dimensional model of the ATLAS planar pixel sensor for the insertable b-layer and the super-LHC upgrade have been studied. The parameters influencing the breakdown behavior were studied using a finite-element method to solve the drift-diffusion equations coupled to Poisson's equation. Using these models, the number of guard rings, dead edge width and sensor's thickness were modified with respect to the ATLAS actual pixel sensor to investigate their influence on the sensor's depletion at the edge and on its internal electrical field distribution. The goal of the simulation is to establish a model to discriminate between different designs and to select the most optimized to fit the needs in radiation hardness and low material budget of ATLAS inner detector during super-LHC operation. A three defects level model has been implemented in the simulations to study the behavior of such sensors under different level of irradiation. Using the results of our simulations, we propose guidelines for the design of future pixel sensor structures and propose test structures to be inserted in a wafer production to verify and calibrate our simulation model.

1 Introduction

The ATLAS detector is a toroidal set of nested detectors. ATLAS is composed of an inner silicon tracker, a transition radiation detector and a calorimetry system designed to observe the products of subatomic reactions occurring during the collisions of up to 7 TeV energy protons at the LHC. The goal of the ATLAS detector is to study the Standard Model with unpreceded accuracy, test the Higgs mechanism and explore physics beyond the Standard Model. ATLAS pixel tracker is located at the center of the ATLAS experiment, close to the interaction point. It consists of a set of three concentric cylinders of silicon pixel sensor modules, disposed as shown in Fig. 1.

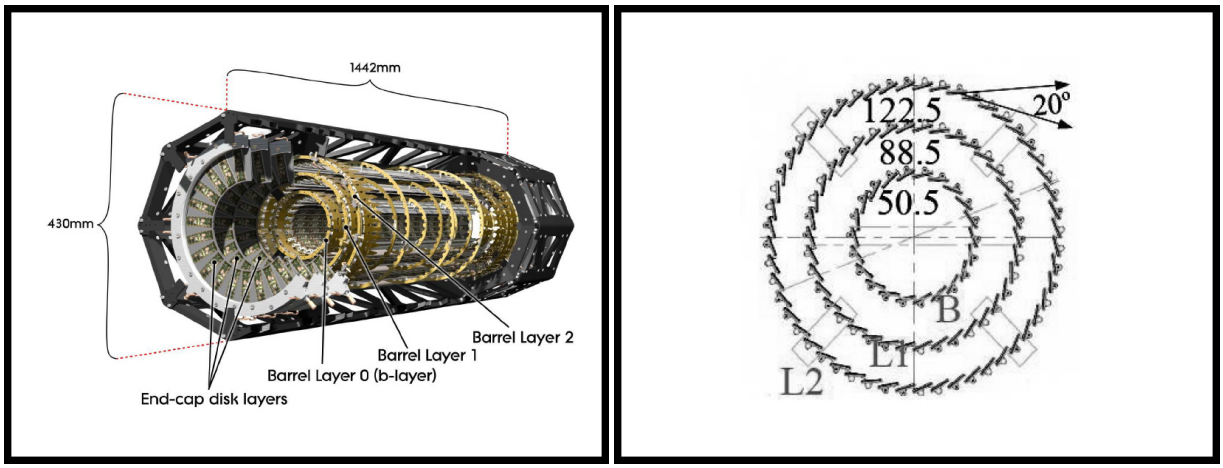

Figure 1: ATLAS pixel detector : 3D view of pixel sensor module support structure (left), r-phi cross-section of ATLAS pixel detector (right)

The inner layer of the ATLAS pixel detector will be exposed to a fluence of $2.43 \times 10^{14}\ n_{eq}/cm^2$ after a year of operation [1] for $100\,fb^{-1}$ integrated luminosity. A replacement of the inner detector, unable to withstand that rate of irradiation after 3 years of operation , will be necessary for the operation of the ATLAS detector at late LHC and super-LHC regime [2]. A new pixel sensor will be required for the inner layer to deliver sufficiently high signal after high level of irradiation. Consequently, its associated electronics will require to process low signal and trigger at very low threshold. It is also desired to reduce the thickness of the inner detector to reduce its influence on Bremsstrahlung photons produced by electrons crossing the inner layer and to reduce the leakage current and the needed operation bias voltage. Finally, limited budget and resources makes cost versus efficiency a major factor to consider in the choice of the ATLAS new inner detector.

Technology computer-assisted design (TCAD) uses our present knowledge of the partial differential equations describing charge carrier's motion and interactions with the crystal lattice in semiconductors, coupled to finite element method to simulate the electrical parameters of the device. This method can be used to explore different designs of the device before its production and optimize its electrical parameters. We used this method to explore different possible designs for the new ATLAS planar pixel. The influence of many design parameters as the number and spacing of guard rings, the sensor's thickness and inactive edge width on sensor electrical characteristics, based on simulation, are presented. A simple model for radiation damage has also been implemented to simulate its effect on the electrical parameters of the device. From our simulation results, we suggest guidelines for the design of future pixel prototypes and propose test structures to be inserted in the wafer production to verify and calibrate our simulation model.

2 Theory

2.1 Transport equation

The dynamics of charge carriers in semiconductors like silicon is well described by the drift-diffusion equations (1), (2), coupled to the Poisson equation (3) [3]:

$$\frac{dp}{dt} = \nabla \cdot D_h \nabla p + \nabla \cdot (p\mu_h \vec{E}) + G_h - \tau_h \tag{1}$$

$$\frac{dn}{dt} = \nabla \cdot D_e \nabla n - \nabla \cdot (n\mu_e \vec{E}) + G_e - \tau_e \tag{2}$$

$$-\nabla^2 V = \nabla \cdot \vec{E} = \frac{\rho}{\varepsilon} \tag{3}$$

$$\vec{J_{disp}} = \varepsilon \frac{\partial \vec{E}}{\partial t} \tag{4}$$

where p et n are respectively the density of holes and electrons in $[\frac{1}{cm^3}]$, D, their respective diffusion coefficient in $[\frac{cm^2}{s}]$, μ the mobility in $[\frac{cm^2/Vs}{m*s}]$. G is the generation rate and $\tau_{e,h}$, the recombination rate, both in $[\frac{1}{cm^3 s^1}]$. The h and e subscript respectively refer to holes and electrons. ρ is the net charge density in $[\frac{C}{cm^3}]$, where C are Coulomb. $\vec{J_{disp}}$ is the displacement current density in $[\frac{C}{cm^3 * s}]$ that needs to be considered in the transient solution. ε is the material dielectric constant.

This system of equations represents a good approximation to describe the behavior of charge carriers in devices with a size of the order of a micron or more. It does not explicitly considers momentum and energy conservation of carriers. A more accurate model, the energy balance equation system, which includes an explicit treatment of these conservation laws, could be used if the drift-diffusion equations were failing in their predictions. Both system of equations are different orders of approximation of the Boltzmann transport equation system that completely describe carrier statistics in the effective mass approximation (EMA).

2.2 Carrier statistics

The model used to represent the density of state at equilibrium for free carriers, n and p, is Boltzmann statistics, which is valid when Fermi energy level E_f is negligible in front of $k_b T$, as it is the case for our simulation. k_b is the Boltzmann constant and T the temperature.

$$n = n_i e^{\frac{(E_f - qV)}{k_b T}} \tag{5}$$

$$p = n_i e^{\frac{(qV - E_f)}{k_b T}} \tag{6}$$

where n_i the intrinsic carrier concentration and q the elementary electric charge.

2.3 Generation-Recombination term

Generation/recombination terms are important to describe the behavior of silicon sensors. Generation is responsible for leakage current present in reverse-biased sensors. Recombination is important to describe the transient behavior of the device after perturbation by a charged particle crossing the depleted bulk. Silicon being an indirect gap semiconductor, generation and recombination occurs mostly through the defect states that are present in the band gap of silicon. The model used in the simulation is the

Shockley-Read-Hall Generation-Recombination [3], which describes the generation-recombination in indirect-band gap semiconductors as silicon. This model assumes that the transition of carriers between bands occurs through a single trap energy level located deeply in the gap, E_{trap}.

$$R_{SRH} = \frac{pn - n_i^2}{\tau_p[n + n_i e^{\frac{E_{trap}}{k_b T}}]\tau_n[p + n_i e^{\frac{-E_{trap}}{k_b T}}]} \tag{7}$$

$$\tau_n = \frac{\tau_{n0}}{1 + \frac{N_{dopant}}{N_{SRHn}}} \tag{8}$$

$$\tau_p = \frac{\tau_{p0}}{1 + \frac{N_{dopant}}{N_{SRHp}}} \tag{9}$$

Equation (7) gives the Concentration-Dependent Shockley-Read-Hall Generation-Recombination model used in our simulation, where (8) and (9) explicit the concentration dependence. τ_{p_n} are the recombination lifetime for holes and electrons, $N_{SRHp,n} = 5 \times 10^{16}\ cm^{-3}$ a material dependent empirical parameters and N_{dopant} the dopant concentration. $\tau_{n0}, \tau_{p0} = 10^{-7}\ s$

2.4 Defects and impurities

High resistivity silicon used for sensors is not a pure material. The presence of oxygen and other impurities affects its electrical properties. Dopant are also introduced during fabrication of the sensors whereas defects are introduced by high energy particles crossing the sensor. In the super-LHC environment , ATLAS inner tracker will be exposed to high level of radiation and the large introduction of structural defects must be taken into account in the design of the sensors. More sophisticated simulations of bulk properties like leakage current would require a more complex description of generation-recombination mechanisms that not included in our simulation. Bulk material is simply represented by its resistivity and generation-recombination is parameterized by radiation damage and standard Shockley-Read-Hall recombination.

Our simulation includes a modified Shockley-Read-Hall Generation-Recombination model that takes into account the presence of multiple trap levels in the band gap, introduced by radiation. The same model could be used to obtain an accurate simulation of bulk properties of different types of silicon. Generation-Recombination terms for each trap are calculated using (7) and a global term R_{total} is calculated following (10).

$$R_{total} = \sum_{\alpha=1}^{l} R_{D_\alpha} + \sum_{\beta=1}^{m} R_{A_\beta} \tag{10}$$

$$\tau_{n,p} = \frac{1}{N_t v_{th,n,p} \sigma_{n,p}} \tag{11}$$

l and m are the numbers of donors and acceptors traps,$R_{A,\beta}$ $R_{D,\alpha}$ the Generation-Recombination terms for respectively acceptors and donors traps. The density of traps N_t is taken into account through the parameters τ_n and τ_p used for each trap level, as shown in (11) .

Finally, charge states of traps are taken into account in Poisson equation right term. The amount of ionized trap is determined using Boltzmann statistics.

Radiation damage introduces defects in the bulk of the silicon that modify its behavior. A model of defect energy state distribution reproducing the behavior of irradiated sensor exists [4] [5], based on the work of CERN ROSE and RD50 collaboration [6–10]. The model allows to reproduce the depletion bias voltage , the double peak in the electric field after irradiation and space charge sign inversion for

n-bulk sensors [11] [12] [13] . Many variation of this model exist to adapt to different bulk material characteristics. For these simulations we used the parameters described in table 2.4

Table 1: Defect energy and capture cross-sections used in SILVACO TCAD software irradiation simulations for n-type silicon

Energy (eV)	Type	$\sigma_n\,(cm^2)$	$\sigma_p\,(cm^2)$	$\eta\,(cm^{-1})$
$E_c - 0.42$	*Acceptor*	2.11×10^{-16}	2.11×10^{-15}	1
$E_c - 0.45$	*Acceptor*	2.11×10^{-16}	2.11×10^{-15}	0.4
$E_c - 0.55$	*Acceptor*	1×10^{-15}	1×10^{-16}	0.08
$E_v - 0.36$	*Donor*	1×10^{-16}	1×10^{-15}	1

$\sigma_{n,p}$ are the electrons and holes capture cross-section and η the introduction rate. The defect density of state (ρ in cm^{-3}) as a function of fluence (ϕ in n_{eq}/cm^2) is calculated following equation 12 .

$$\rho = \phi * \eta \tag{12}$$

2.5 Impact ionization

In the super-LHC environnement, the inner detector will suffer from radiation damage. One of its effect is the increase of the bias voltage needed to keep a good signal to noise ratio. High bias voltage must be used to operate the sensors in over-depletion. The high voltage drop on the sensors results in high electrical field inside the silicon bulk. When the electric field is sufficiently high, breakdown can occur due to acceleration of free carriers: accelerated electrons ionize surrounding atoms creating an avalanche. Equation (13) describes how to compute the impact generation term G_{impact} as a function of current densities $\vec{J_{n,p}}$ and electric field $\vec{E}$. Various expressions exists for the $\alpha_{n,p}$ term. The Selberherr's Impact Ionization Model (14) [14] has been used to account for impact ionization in our simulations.

$$G_{impact} = \alpha_n(\vec{E}) \left|\vec{J_n}\right| + \alpha_p(\vec{E}) \left|\vec{J_p}\right| \tag{13}$$

$$\alpha_{n,p}(\vec{E}) = A_{n,p} e^{-\frac{B_{n,p}|\vec{J_{n,p}}|}{\vec{E}\cdot\vec{J_{n,p}}}} \tag{14}$$

Coefficients $A_{n,p}$ and $B_{n,p}$ are determined experimentally and are chosen as a function of the material.

2.6 Boundary conditions

To solve our set of differential equations we need to restrict ourselves to a solution in a bounded domain, the sensor. We must choose boundary conditions reflecting the properties of the system we want to simulate. Three types of boundaries were used during our simulation, representing the oxide-Silicon interface, the electrode interface, and the periodicity boundary. In addition we need a model for the cutting edge of the sensor.

The boundaries between silicon dioxide and silicon is a semiconductor/insulator boundary characterized by the presence of an accumulated charge layer at the interface. The boundary condition applied to these surfaces for the Poisson equation is the Neumann boundary condition (15) that takes into account the charge layer (ρ_s) present at the surface . Also, electrons and holes concentrations are set to zero on this boundary and the current is not allowed to flow through this surface.

$$\hat{n} \cdot \varepsilon_1 \vec{\nabla}\Phi_1 - \hat{n} \cdot \varepsilon_2 \vec{\nabla}\Phi_2 = \rho_s \tag{15}$$

Metal-semiconductor surfaces are the boundaries between the silicon bulk and the metallic electrodes. This is usually a ohmic contact and the current is allowed to flow through them. The voltage Φ is constant and equals the bias voltage applied to the sensor by an external power supply. The concentration of carriers (p_s,n_s) at the surface of the contact is determined by equations (16), (17), derived for Boltzmann's statistics, knowing the bias voltage applied at the electrodes. The effect of the contact work function is considered negligible as highly doped regions are located below the electrodes.

$$n_s = \frac{1}{2}[(N_D^+ - N_A^-) + \sqrt{(N_D^+ - N_A^-)^2 + 4n_i^2}] \tag{16}$$

$$p_s = \frac{n_i^2}{n_s} \tag{17}$$

Where N_D^+, N_A^- are the ionized donors concentration and ionized acceptors concentration in cm^{-3}.

Guard ring structures are metal semiconductor interfaces where the metallic electrode self-biased. To represent this case, we must impose a fixed bias voltage and a null current flow on this contact. The bias voltages taken by the floating contacts are then found starting from an initial guess, using an iterative method.

To reduce the size of the problem to be solved, we can use periodicity boundary conditions using geometric properties of the sensor. In our simulation, we will be interested to the solution on the sides of the sensor. Knowing the solution will become periodic in the X-Y plane when approaching the center of the device, we can cut our model at a distance of the edge large enough to consider the solution will become periodic at this point. We then impose the periodicity condition (18) at the surface for electrons and holes concentration and for the bias voltage.

$$\begin{aligned} \vec{\nabla} V \cdot \hat{n} &= 0 \\ \vec{\nabla} n \cdot \hat{n} &= 0 \\ \vec{\nabla} p \cdot \hat{n} &= 0 \end{aligned} \tag{18}$$

Where $\hat{n}$ is the unitary normal vector of the boundary.

3 Simulation goals

This section details the different characteristics of the sensors we want to simulate and the data we can extract from the simulation results to obtain information on the possible behavior of real sensors.

3.1 Depletion

Depletion voltage is an important parameter of semiconductor sensors. As the bias voltage on the sensor's electrode increases, the amount of free carriers in the sensor bulk is reduced, up to the point where all the carriers are gone and the depletion region extends to both faces of the sensor. The bias voltage where this condition is reached is the depletion bias voltage (V_{fd}). In pixel sensors, the signal generated by electron-hole pairs generated by ionizing particles (1 pair generated for 3.6eV of deposited energy) crossing the sensor is proportional to the length of the track in the depleted bulk of the sensor. Under-depleted or undepleted pixels will collect less or no charge when crossed by a charged particle. Therefore it is important to operate the pixel sensor at a bias voltage higher that the depletion voltage. In addition, radiation damage caused by exposition to high particle fluences will modify the depletion bias voltage, given by equation (19), by changing the effective dopant concentration in the bulk, following equation (20) [15]. For highly irradiated sensors ($> 10^{15}\ n_{eq}/cm^2$) as in the case of the Insertable b-layer at its end of life, depletion bias voltage will become a less important parameter as trapping of charge will reduce

greatly the mean free path of electrons in the bulk of the sensor. However, charge deposited at a distance from pixels superior to the mean free path of electrons will still induce a signal on the pixel making it still desirable to operate the sensor as depleted as possible.

$$V_{dep} = \frac{q}{\varepsilon\varepsilon_0}|N_{eff}^2|d^2 \tag{19}$$

$$N_{eff}(\phi) = N_A(\phi) + N_Y(\phi) + N_{eff0} * (1 - e^{-c\phi}) + g_c\phi \tag{20}$$

where N_{eff} is the effective dopant concentration, ϕ the fluence, c and g_c are material specific constants and N_A and N_Y the annealing and reverse annealing terms. To determine the depletion voltage in a simulation, we plot the quasistatic capacitance versus $(1/\Phi)^2$. The inflexion point of the graph is the depletion bias voltage.

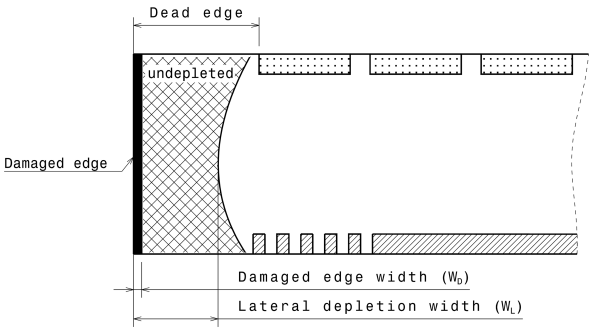

Figure 2: Lateral depletion at the edge of the sensor

Lateral depletion width W_L is another related parameter that tells us the distance between the sensor's edge and the lateral border of the undepleted region. This has proven to be important to predict the occurrence of lateral breakdown between the outermost pixel and the guard ring structure. Edges of sensors are characterized by a high concentration of defects. The cutting of the sensor, its oxidation and the diffusion of impurities damage the lattice on a certain depth W_d (fig. 2), that is dependent of the dicing method used to cut the sensor from it originating wafer. If the electric field reaches this zone ($W_L < W_d$), the high density of defects could increase the generation term of the drift-diffusion equation, generating high leakage current and eventually breakdown [16]. It should be noted that a small electric field present at the edge could be tolerated as long as the generated leakage current do not compromise the operation of the sensor. In our simulation, we pay close attention to the determination of W_L to ensure it is larger than the W_D associated to the sensor's dicing method.

3.2 Electric field shape and magnitude

The electric field shape inside the bulk of the sensor is an important parameter to determine its charge-sharing behavior and its typical pulse shape. The free carriers move in the electric field and its magnitude influences the speed at which the charge is collected. Most importantly, as mentioned before, electric field magnitude tell us about the probability of breakdown due to avalanche formation. Breakdown electric field in silicon is in average close to $|E_{break}| = 3 \times 10^5\ V/cm$. As a rule of thumb, we assume that the field must be under $0.5\ |E_{break}|$, with a 0.5 safety factor. For a safe operation of the sensor, our model should not present a field magnitude over this limit. As mentioned before, impact ionization has been implemented in the model to take into account the effect of high electric field in the production of leakage current in the device and the formation of possible breakdown.

3.3 Leakage current

The bulk current present between the electrodes of a sensor under bias, the leakage or dark current, is strongly dependent of the generation term of the drift-diffusion equation, hence, of the amount of defects in the bulk of the sensor. We can simulate how leakage current is affected by the amount of defects present in the bulk. The leakage current is often described as proportional to the depletion width (W) and to the inverse of the generation lifetime (τ_g) [15]. This current is given by the power supply applying the bias on the sensors and determines power dissipation in our sensors. This current also adds up to the signal when a particle is detected, increasing the noise and reducing the energy and position resolution of our sensor. It is important to keep its value as low as possible and route this current to the guard rings if possible to reduce leakage that passes through the pixels and ensure a good performance of our sensors. In our simulation, we computed the I-V curve for each electrode of our model to keep track of this parameter.

4 Simulated model

Our goal in this simulation is not to reproduce in details the behavior of the ATLAS pixel sensor, but to extract tendencies and offer guidelines for the design of future sensors. Hence, we simplified our model by using a 2D simulation geometry represented in fig. 3. This model remains valid as we consider the sensor to be half-infinite and symmetric in the YZ plane. We have built a parametric model of the sensor that can be used to explore its behavior while changing the different characteristics of the model. By reducing the size of our model comparatively to the real sensor geometry, we obtain a problem that is easily solved in a short computing time ($\propto$ minutes on a standard dual-core cpu machine), which allow us to explore a large range of parameters in a reasonable simulation time.

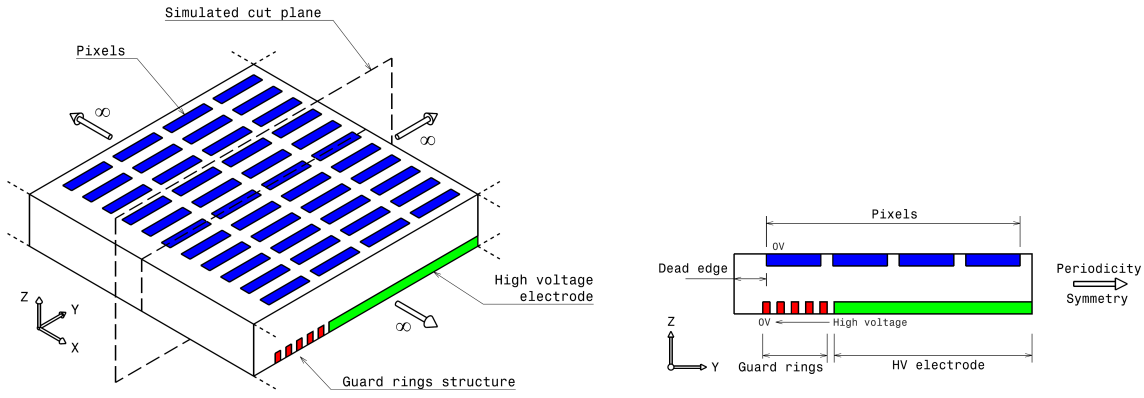

Figure 3: Simulation geometry, 3D view of the idealized sensor (left) and Y-Z simulated plane (right)

4.1 Doping profile

The doping concentration used for our model is taken from ATLAS pixel Technical Design Report [17] for an n-in-n design. The bulk is high resistivity n-type Silicon . The pixel's implant are highly doped n-type and are insulated from each other by low dose p-type implant. Guard ring and high-voltage electrode doping are p-type. Fig. 4 shows the geometrical distribution and numerical values for doping used in our simulation. We chose to use a simplified representation of doping profiles as the exact doping profiles of the sensor are not well known. Doped region are one micron deep and decay exponentially over one

micron outside the doped zone. This is coherent with Monte-Carlo simulation of ion implantation in silicon. This simplifies the problem, hence reducing computing time needed. The goal of our simulation is not to reproduce exactly the behavior of sensors so this level of accuracy is sufficient for our needs.

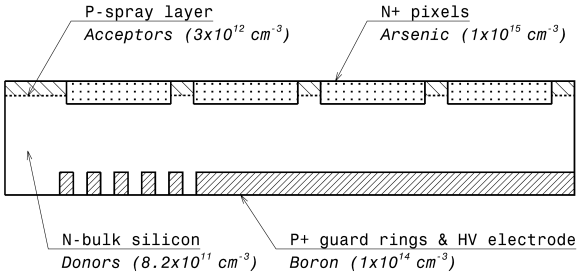

Figure 4: Doping profiles used in our simulation

4.2 Guard Ring structure

The goal of the guard ring structure present next to the high-voltage electrode is to ensure a smooth transition from high voltage to ground while approaching the outer edge of the device. Each guard ring acquire its bias voltage by a punch-trough mechanism forming a smoother transition from high bias voltage to ground at the edge of the sensor. This is needed to ensure that no bias voltage difference exist between the two sides of the wafer, close to the edge. In this condition, no electric field is present at the edge, preventing possible breakdown and excess leakage current [18]. These rings can also be used, if connected to bias, to collect leakage and surface current that would increase the noise in the pixels, becoming a current-terminating structure (CTS) [19]. In ATLAS actual design of the pixel sensor, the number of guard ring is fixed to 16, with a width of 10 microns and a distance between them varying from 15 to 8 microns. A metal overhang of various width is present over the oxide on the high voltage side of the guard rings and serves to control the oxide charge distribution and the electric field present in the oxide. The guard rings represent a dead zone in our sensors, meaning no particle is detected close to the structure. This forced the shingling scheme of sensors in ATLAS tracker to avoid detection gap between sensors. This shingling increase the amount of material present in the tracker and should be avoided to reduce the material budget of the inner detector and increase the simplicity of its configuration. One of the goal of the simulation has been to see how we can modify the number of guard rings and their spacing to reduce the dead zone while maintaining adequate lateral depletion width W_L and lowest possible electric field magnitude near the rings.

4.3 Dead edges

The dicing of pixel sensors from their originating wafer creates structural damage that affects the properties of the edge. A dead edge width must be included in the design, as shown in fig. 2, to exclude this zone from the sensible part of the sensor. This dead edge is added to inactive part of the sensor and must be kept as small as possible.

A special attention must be taken to modelize the dead edge of a silicon sensor. Many models exist to address this problem and each have its weakness that must be taken into account, as presented in the following section.

4.3.1 Oxide charge

Silicon dioxide forms itself naturally when bare silicon is in contact with atmospherical oxygen. A naive model to simulate the edge of the sensor is to assume a Silicon-Oxide boundary at the cutting edge. The weakness of this model is that it does not render the surface conductive as it is expected from experimentation. But for simulation where the dynamics takes place far from the cutting edge, it can be sufficiently accurate to modelize lateral depletion mechanism

4.3.2 Virtual implant

A method to make the edge a conductive surface is to add an implant at the edge to make this region less resistive. As silicon becomes more doped, it becomes more conductive, making it possible to channel some current at the edge. In addition, when this junction get forward biased, a high current is generated , a way to modelize the formation of a lateral breakdown. Junction parameters as dopant concentration and junction depth can be adjusted to reproduce experimental data.

4.3.3 Amorphous Silicon

Dicing mechanism induces structural damages in the Silicon crystal lattice near the cutting region. This induces a process of amorphisation of silicon. Amorphous Silicon is a complex material where no short or long distance orders exists in the crystal lattice. A method to modelize amorphous Silicon is to introduce a high number of defects in the band gap of Silicon. As the crystal lattice of the Silicon is highly perturbated in the cutting edge region, trap states are created by the defects in the crystal lattice that are introduced. To represent such a distribution of defects in the band gap, we use a continuous density of states distribution to describe the band gap defects distribution. This distribution can then be tuned to reflect the behavior of real sensors measured in the laboratory. The generation-recopmbination term related is calculated using an integral form of equation **??** and 10. Equation (21) [20] shows how we describe the defect distribution in the band gap.

$$
\begin{aligned}
&g(E) = g_{TA}(E) + g_{TD}(E) + g_{GA}(E) + g_{GD}(E) \\
&\\
&t_A(E) = N_{TA} e^{\frac{E-E_c}{W_{TA}}} \\
&t_D(E) = N_{TD} e^{\frac{E_v-E}{W_{TD}}} \\
&g_A(E) = N_{GA} e^{(\frac{E_{GA}-E}{W_{GA}})^2} \\
&g_D(E) = N_{GD} e^{(\frac{E-E_{GD}}{W_{GD}})^2}
\end{aligned}
\tag{21}
$$

The density distribution function consists of two exponential tails functions (TD, TA) and two Gaussian function distributions for donors and acceptors (GD, GA) giving the energy distribution in cm^{-3}. Table 2 shows the default parameters used for this model in our simulation. The defect density distribution that is created by these parameters is represented in fig. 5. $E_v = -1.12\,eV$ is the valence band energy and $E_c = 0$ the conduction band energy. The model used in these simulations was proposed by *E. Noschis and al.* [19]

We included the dead edge width as a parameter of our simulation. This allows us to extract the lateral depletion width W_L for different models. Knowing the depth of the damaged zone for different dicing techniques, we can determine the smallest dead edge width possible to keep our sensor protected from lateral breakdown, according to the different models, as explained in section 3.1 . To select between the models and obtain more accurate prediction, test structure will need to be built to verify the prediction associated with the different dead edges models.

Table 2: Default defect density of states distribution parameters in SILVACO TCAD software

Parameters	Values
N_{TA}	$1.12x10^{21}\ cm^{-3}/eV$
N_{TD}	$4.00x10^{20}\ cm^{-3}/eV$
N_{GA}	$5.00x10^{17}\ cm^{-3}/eV$
N_{GD}	$1.50x10^{18}\ cm^{-3}/eV$
E_{GA}	$0.4\,eV$
E_{GD}	$0.4\,eV$
W_{TA}	$0.025\,eV$
W_{TD}	$0.050\,eV$
W_{GA}	$0.100\,eV$
W_{GD}	$0.100\,eV$

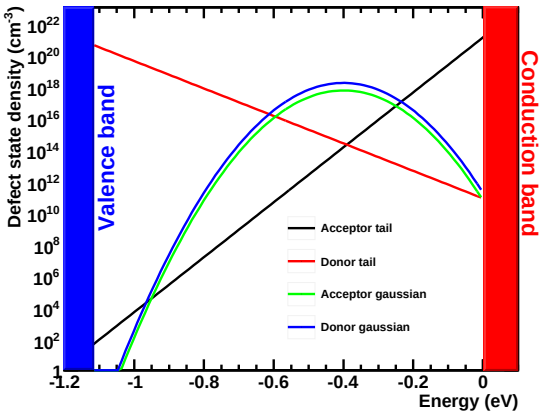

Figure 5: Defect density distribution in the band gap of amorphous silicon used for our simulation

4.4 Sensor thickness

The last parameter of our model is the thickness of the sensor. Current ATLAS pixel sensor exhibit a thickness of 254 microns. However, simulation were performed using a 280 microns thickness to allow easier comparison with sensors that will be available in our laboratory. Reducing the thickness has many advantage in term of radiation hardness in addition to helping reducing the material budget of the inner detector. In our simulation, we explore how thinning the sensor will change the properties of the sensor, in combination with the other parameters described before.

4.5 Mesh

The mesh represent the subdivision of the domain on which we want to solve the transport equation into a set of triangular sub domains on which we approximate the solution to the system of equation as a second order polynomial function. To obtain a good accuracy, these domains must be small enough so the real solution of the system of equation in the domain is locally polynomial on each sub domain. Each mesh point represent a degree of freedom in the problem to solve. The complexity of the matrix to invert

for this kind of problems in two dimensions increase as $(dof)^2$. We performed convergence studies on the models we used in this work to optimize the mesh and keep a refined mesh only in regions of interest like the doping and the edge and a coarser one in region like the bulk where the parameters we solve (n, p, ϕ) are locally polynomial even on long distance.

5 Results

For this simulation study, we decided to concentrate on exploring the feasibility of reducing the inactive surface of planar pixel sensors by reducing the number of guard rings and the width of the dead edge left on the side for protection. We will present simulation of the current design and explore how the reduction of the dead edge width, of the number of guard rings or the thinning of the sensor can help reducing the inactive area of planar pixel sensors. Simulation of irradiated sensors was limited to a fluence of 10^{14} n_{eq}/cm^2 as this is the maximum fluence at which the radiation damage model has proven to be accurate. Further work on this model will be performed on this model using calibration with experimental data to extend its validity to higher fluences.

5.1 Current ATLAS planar pixel sensor design

Simulation of the current ATLAS planar pixel sensor design was performed up to 500 V for unirradiated and irradiated sensors. The 3 defects energy level model has been used to simulate radiation damage [4, 5]. Fig. 6 shows the simulated bias voltage for the Actual ATLAS pixel design. Four pixels are included along with the guard rings (to the left of the figures). As fluence seen by the sensor increase, the space charge sign invert and depletion occurs from pixel toward the backplane like in a n-in-p sensor design.

Fig. 7 shows the electron concentration in the sensor for different fluences. Space charge sign inversion has for effect that holes gradually replace electrons as the majority carrier. This is shown in fig. 8 representing hole concentration increasing as electron concentration decrease, mainly in the undepleted region. The undepleted volume for an unirradiated sensor extends on 480 microns from the edge of the sensor. This width is retained until space charge sign inversion but it is unclear what occurs after space charge sign inversion at the edge of the sensor.

Fig. 9 shows the simulated voltage distribution on the guard ring structure after exposition different fluences. Guard ring takes their bias voltages as the depletion region of the sensor reaches them. After space charge sign inversion, depletion occurs from the pixel side and may never completely reach the guard ring side of the sensor. This cause the guard ring to be less effective to control the bias voltage drop as space charge sign inversion occurs.

Each simulation was performed to 500 V bias voltage and no breakdown occured. However, not all details have been included and other processes not included in the simulation could trigger a breakdown at lower bias voltage. The highest electrical field is present at the edge of the high voltage electrode and at the surface of the inter-pixel region.

5.2 Dead edge reduction

Simulation have been performed to explore the possibility to reduce the dead area of the sensor that span from the edge to the first guard ring. Simulation for an edge of 100, 200, 300, 465 microns (actual design) have been performed. Fig. 10 shows the electron concentration for an unirradiated sensor with different dead edge width.

To see how edge behavior change after space charge sign inversion, we simulated the same models after being irradiated up to $1e14$ $n_{eq}cm^{-2}$. Fig. 11 shows the hole concentration for the same simulated

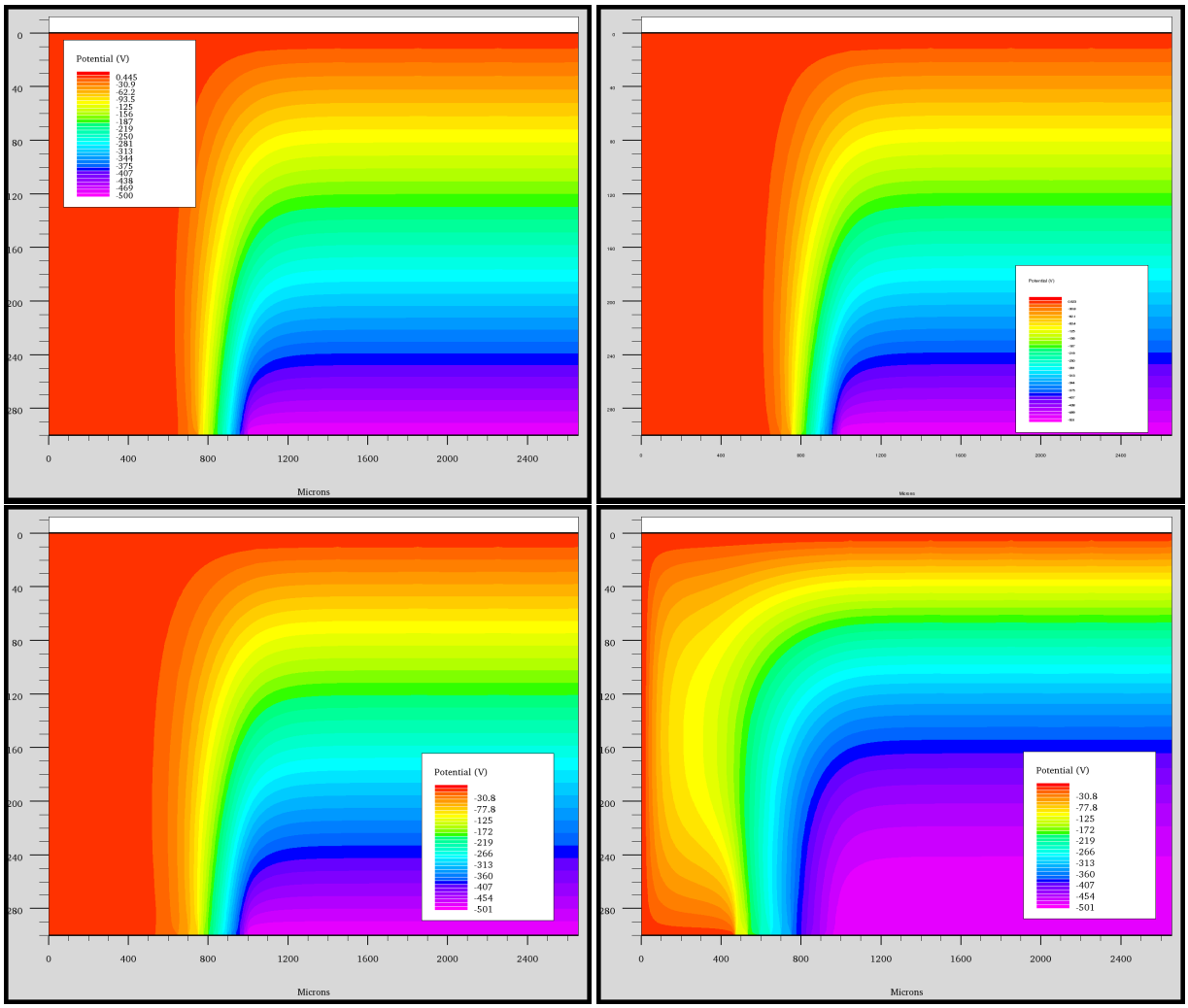

Figure 6: Simulated 2D voltage profile for ATLAS pixel sensor (300 μm thickness, 2500μm width), unirradiated (upper left), 1e12 $n_{eq}cm^{-2}$ (upper right), 1e13 $n_{eq}cm^{-2}$ (bottom left), 1e14 $n_{eq}cm^{-2}$ (bottom right), Minimum= 0V maximum=-500V

geometry. The complex behavior after irradiation makes it difficult to define depletion. Next, fig. 12 shows the magnitude of the electric field after irradiation . We observe that a small electric field is present at the edge and increase with smaller dead edge width. It is unclear from the model implemented what would be the behavior of sensors at the edge after irradiation. Further investigation with test structure should be done to investigate further the signification of the obtained results.

5.3 Reducing the number of guard rings

The guard rings structure represent inactive area of the sensor and must be reduced, The actual ATLAS pixel sensor has been simulated with 0,1,3,4 of the outer guard ring removed.

Fig. 13 shows the bias voltage distribution taken by the guard rings for the different simulated structures with an applied bias of 500 V. It is shown that the bias voltage of the guard rings are almost the same as before their removal, with the outer guard rings moving closer to ground while never reaching it.

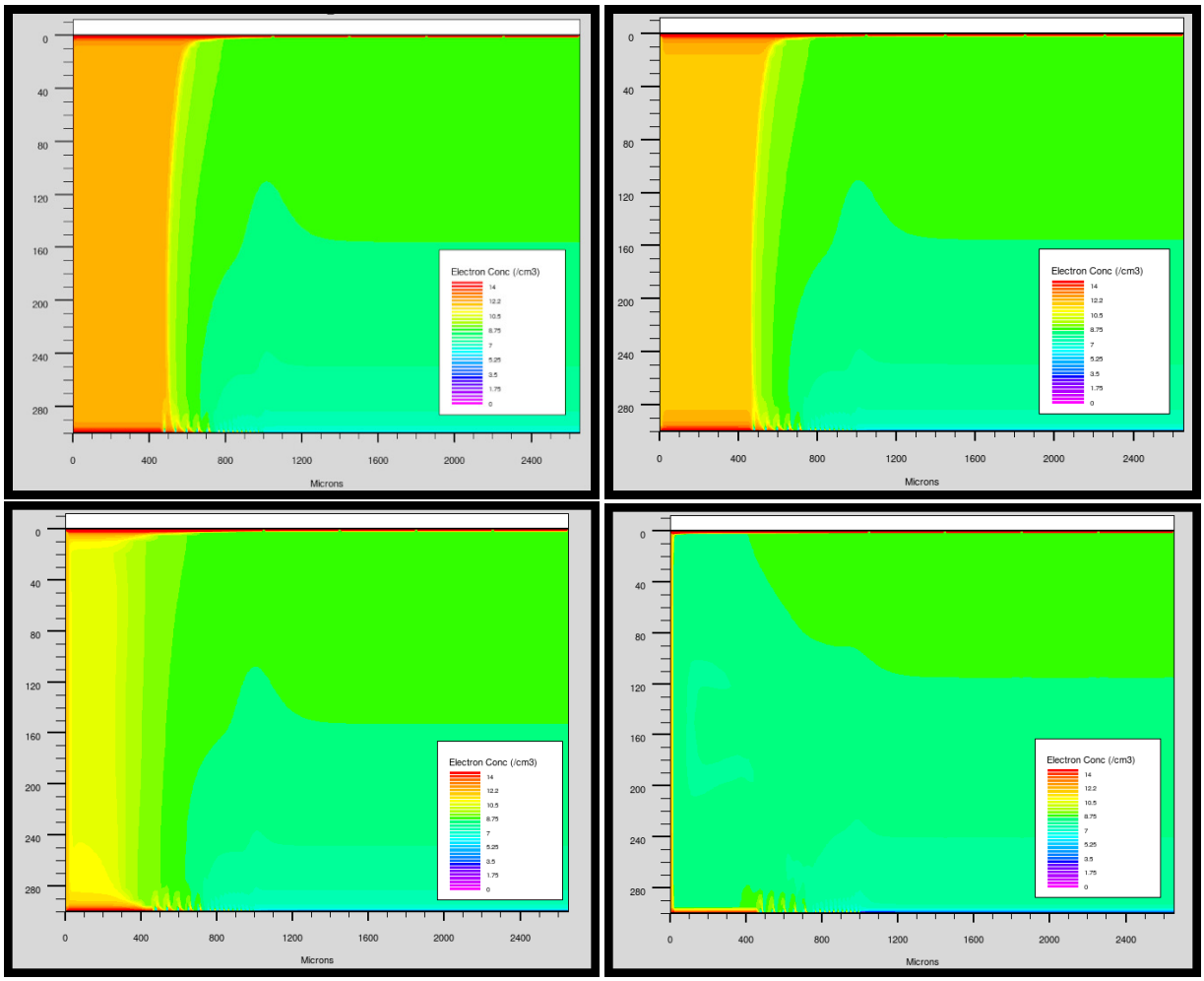

Figure 7: Simulated 2D electron concentration profile for ATLAS pixel sensor (300 μm thickness, 2500μm width) , unirradiated (upper left), 1e12 $n_{eq}cm^{-2}$ (upper right), 1e13 $n_{eq}cm^{-2}$ (bottom left), 1e14 $n_{eq}cm^{-2}$ (bottom right), minimum=0 maximum =1e14 cm^{-3}

Fig. 14 shows the electric field distribution at 0.1 μm under the guard rings for the different simulated structures with an applied bias of 500 V. The high peak next to outer guard ring is due to the rapid bias voltage drop from outer guard ring to passivated edge.

5.4 Thinning of the sensor

Thinning of a pixel sensor can be beneficial to a detector in high fluence environnement. Charge collection occurs in a small region leaving most of the sensor useless. Lower bias voltage is needed and trapping is reduced due to small travel distance of holes and electrons in the bulk. We performed simulation with the actual ATLAS pixel design with a thickness of 100,200 and 300 μm. Fig. 15 shows the electron concentration for the 3 performed simulation. Lateral depletion at half-height, defined as the distance from edge where the silicon is undepleted, is 700 μm for the 100 μm thick model, 540 μm for the 200 μm thick model and 480 μm for the 300 μm thick model. The guard ring structure begins at 470 μm in the same coordinated system.

For a fixed bias voltage, we notice that the depletion is more complete in the thinner sensor as the electric field is higher. This means that a thin sensor could be operated at lower voltage. A more elaborate

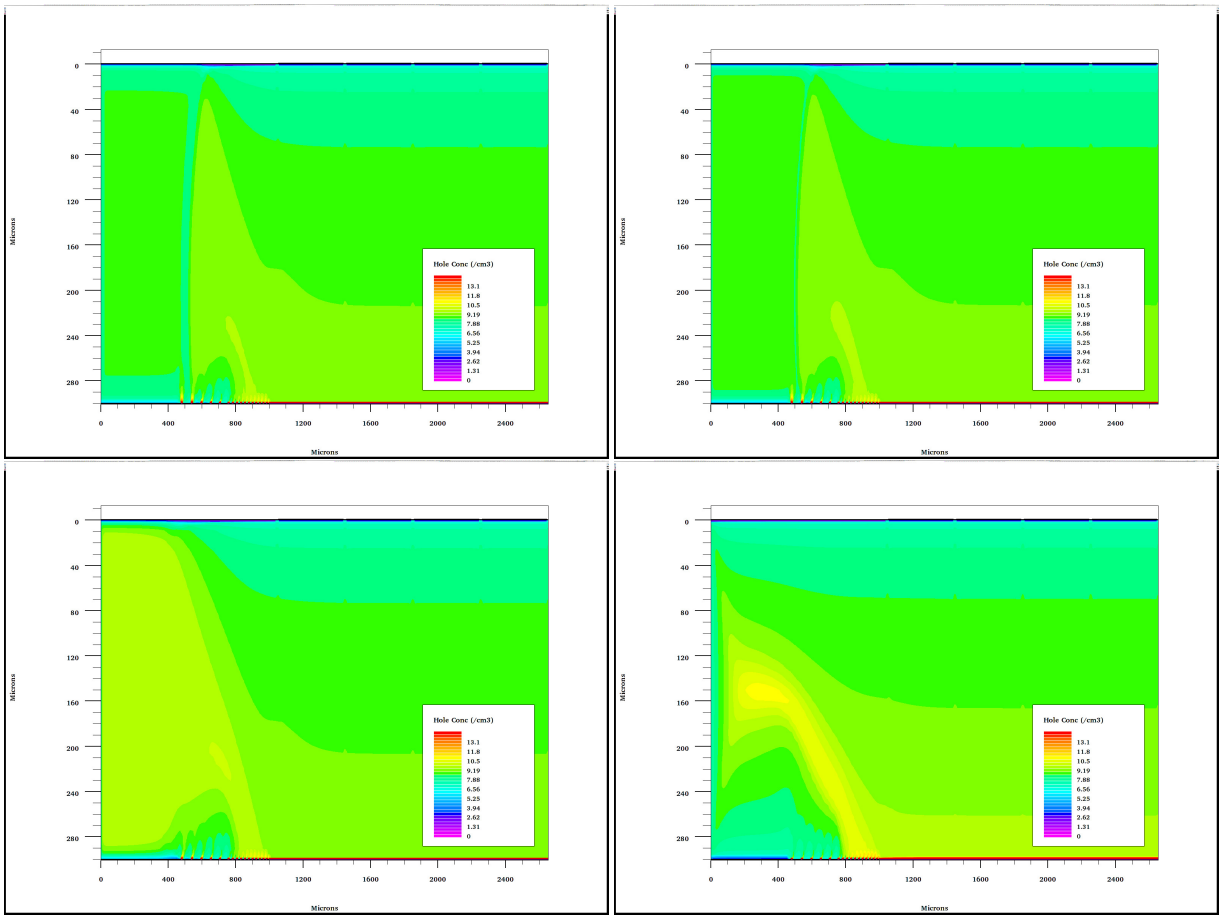

Figure 8: Simulated 2D hole concentration profile for ATLAS pixel sensor (300 μm thickness, 2500μm width), unirradiated (upper left), 1e12 $n_{eq}cm^{-2}$ (upper right), 1e13 $n_{eq}cm^{-2}$ (bottom left), 1e14 $n_{eq}cm^{-2}$ (bottom right) , minimum=0 maximum =1e14 cm^{-3}

sensor thinning simulation study is also foreseen in the future.

5.5 Space charge sign inversion (SCSI)

For our actual ATLAS sensor design, we simulated the CV curve to determine the depletion bias voltage of the model and verify that the model reproduce the space charge sign inversion that will occur in ATLAS pixel sensor submitted to super LHC fluences. Fig. 16 shows the depletion bias voltage of the sensor, for a 2.4 $k\Omega cm$ FZ n-type sensor, as a function of fluence. We observe a behavior similar to the prediction of the Hamburg model, represented by the black line, fitted here on simulation data ($g_c = 0.0260 \pm 0.0002$). This verify that the model used for previous simulation is consistent with the scenario predicted from experimentation for LHC and super LHC inner detector pixel sensors.

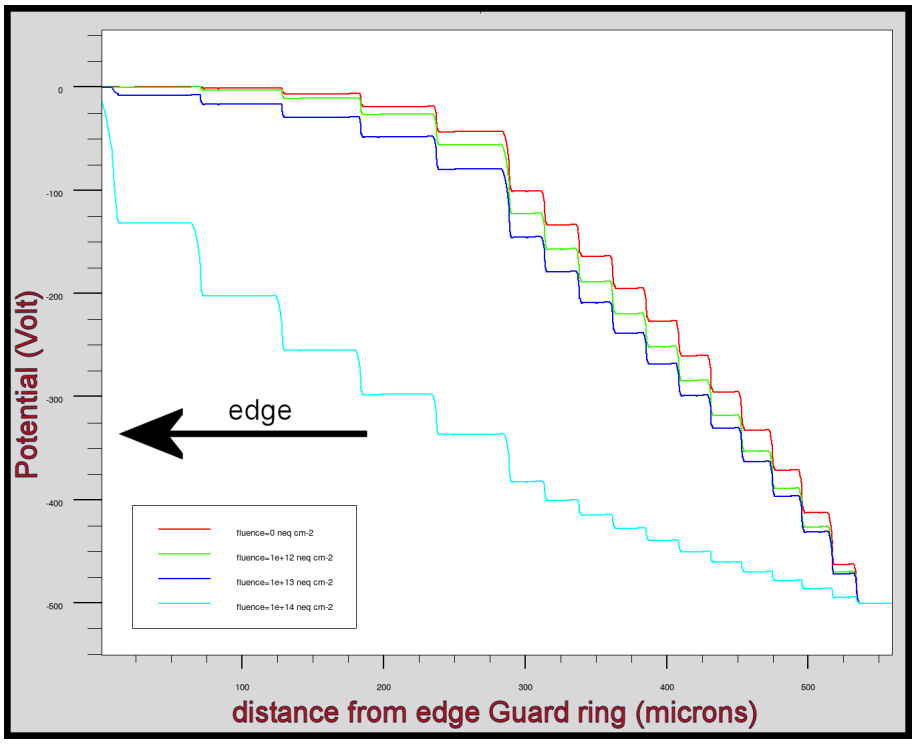

Figure 9: Potential distribution of the guard ring structure for different fluences, unirradiated (upper left), $1e12\ n_{eq}cm^{-2}$ (upper right), $1e13\ n_{eq}cm^{-2}$ (bottom left), $1e14\ n_{eq}cm^{-2}$ (bottom right), minimum =0, maximum =2.5e5 V/cm

6 Discussion

6.1 Edge reduction

Simulations performed in this work show that for unirradiated sensors, the lateral depletion of the current ATLAS pixel sensor design biased at 500V is sufficient to protect the edge of the sensor from lateral breakdown. The choice of a large edge width was conservative choice made to keep a safety margin. Simulation shown in section 5.2 show that the edge width could be reduced to 100 μm while keeping an undepleted zone at the edge of the sensor that is sufficient to protect against damage at the edge. New laser cutting or plasma etching technologies could be used to reduce the thickness or the damaged area at the edge of the sensor, making it possible to safely reduce the edge of the sensor to a smaller value of the order of 100 μm.

6.2 Guard ring reduction

The other approach to reduce the inactive area would be to reduce the number of guard rings in the multi-guard ring-structure. The problem that could arise from this approach would be an augmentation of the electric field profile at the guard ring surface. If potential drop between guard rings or between a guard ring and the edges becomes too high , the electric field might reach breakdown value for silicon. In the simulation we performed, we show how removing up to 4 of the outer guard rings would affect only slightly the electric field distribution under the guard ring. Also, removing a guard ring do not affect much the potential taken by the other guard ring present in the structure. As we can see in fig. 9, the highest potential drop occurs at the fifth outer guard ring. Hence, removing this one would bring a

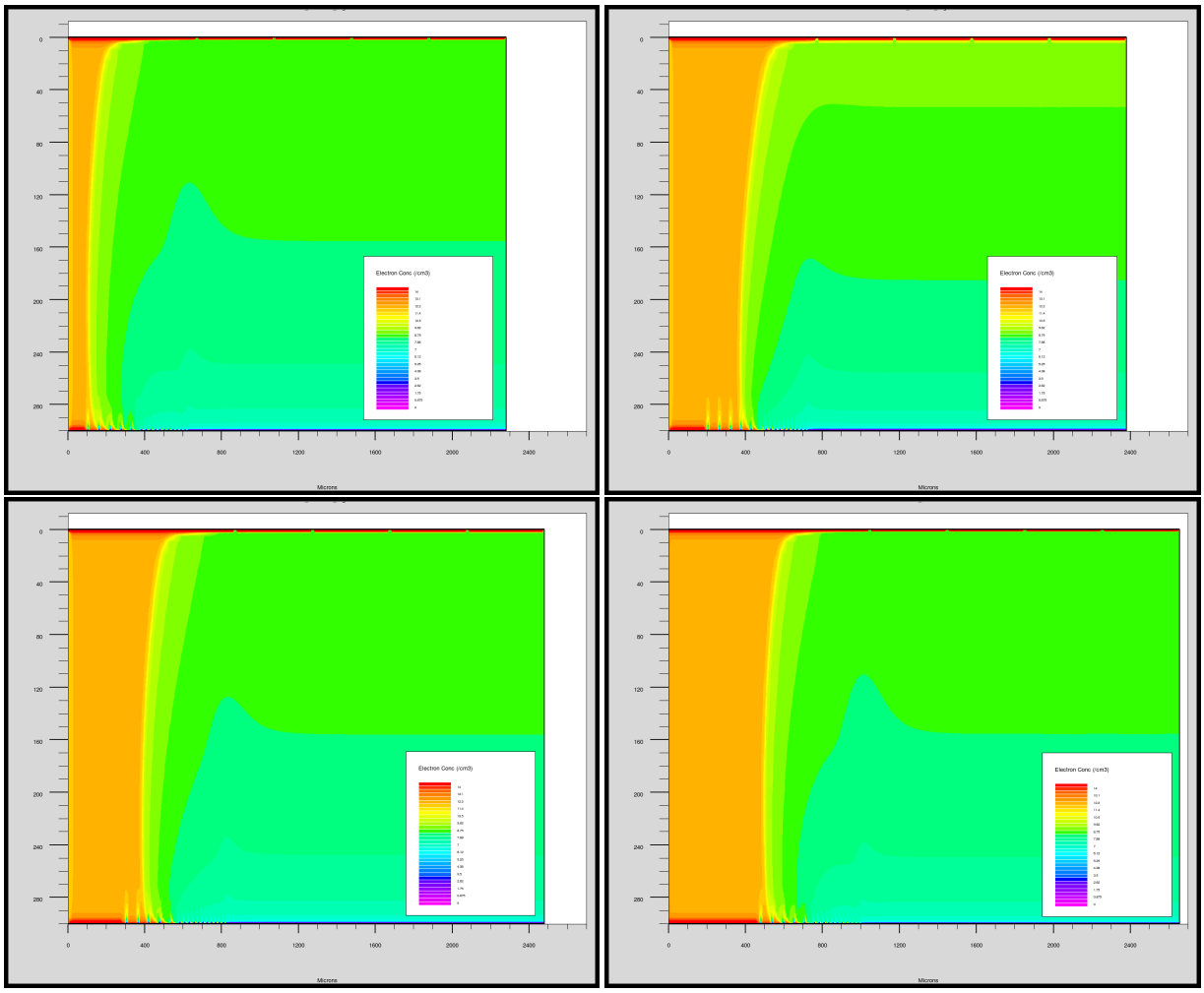

Figure 10: Simulated electron concentration profile for an unirradiated ATLAS pixel sensor for a dead edge width of (from left to right, top to bottom): 100, 200, 300 and 468 microns , minimum=0 maximum =1e14 cm^{-3}

very large potential drop of more than 100V between the outer guard ring and the edge of the sensor. This would be unacceptable as this would add a possibility of breakdown of sensor. This represents an indication that the geometry of a slimmed guard ring structure should be further optimized to be able to operate with such reduced guard rings.

One concern for n-in-n sensor like actual ATLAS pixel design is the behavior of the guard rings after space charge sign inversion. Fig. 9 shows how potential distribution changes as a function of radiation damage. After space charge sign inversion, the outer guard ring become more effective to lower the potential toward the edge while inner guard ring become unnefective. Removing the outer guard rings would allow the inner guard ring, closer to each other, to become effective and would limit the number of ineffective guard ring after space charge sign inversion.

Finally, during this work, it has been noticed that the guard ring behavior is closely linked to the doping profiles and oxide charge values that are used for simulation. To be able to perform accurate simulation of the behavior of real device, we need to be able to compare simulated result to measurement in order to fine tune the model's parameters. Last subsection will discuss the test structures suggested

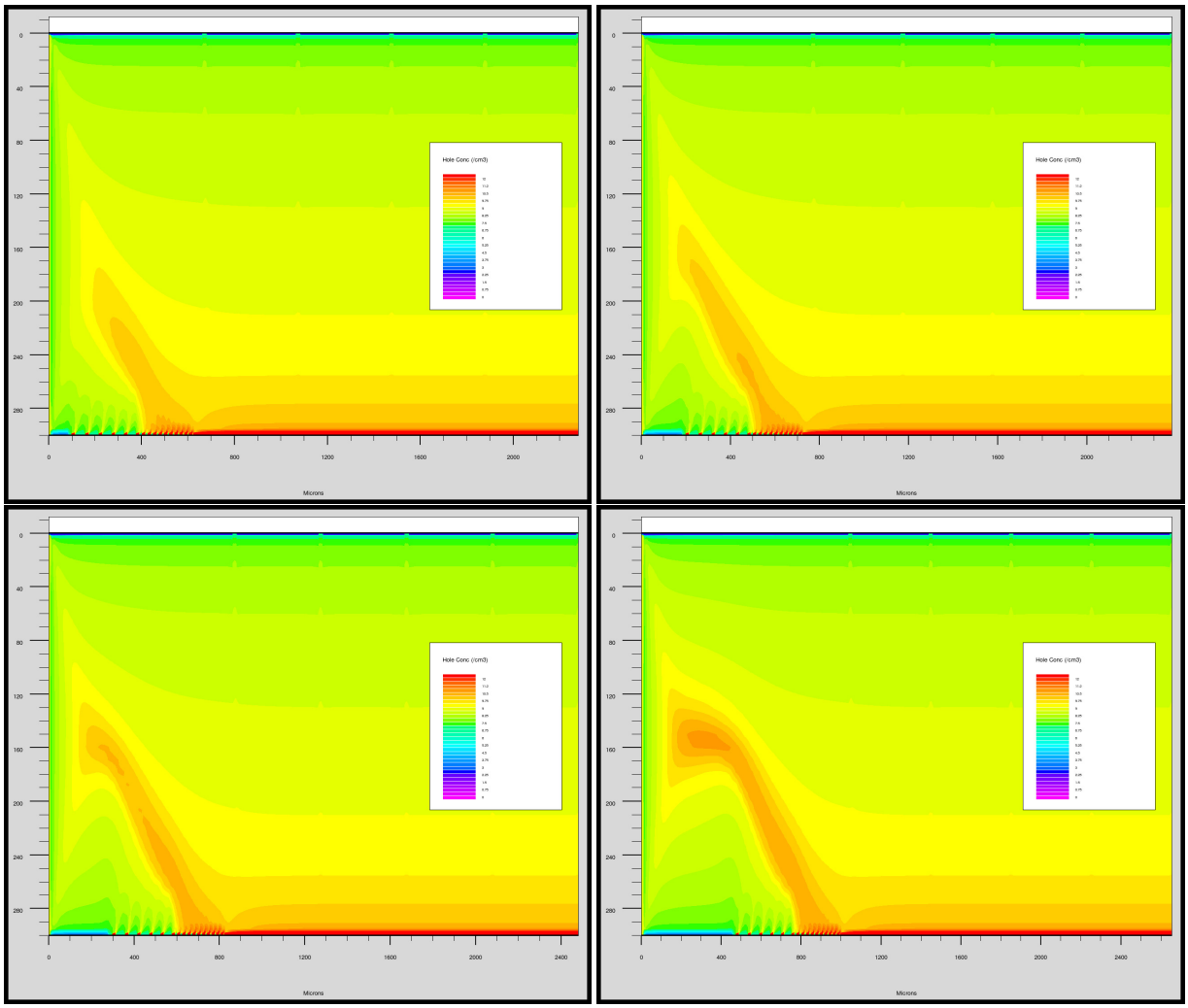

Figure 11: Simulated hole concentration profile for an irradiated ($1e14 n_{eq} cm^{-2}$) ATLAS pixel sensor for a dead edge width of (from left to right, top to bottom): 100, 200, 300 and 468 microns, minimum=0 maximum =1e14 cm^{-3}

for insertion in the wafer production to calibrate our simulation and better understand the guard ring behavior.

6.3 Thinning

Reducing the thickness of the sensor is also an approach that is discussed to improve the sensor behavior after irradiation. Simulation presented here shows that there is no problem encountered using this method to harden the sensor against radiation. It is even beneficial in term of lateral depletion as thinner sensor gets wider undepleted region at the edge than thick sensors. Also, thin sensor can be operated a lower bias voltage to produce full depletion. While depletion is not the most relevant factor for highly irradiated sensors as mean free path of electrons become smaller than the reachable depletion depth, it would be beneficial for the early operation of the Insertable B-layer and would yield to higher signal in late operation as charge drifting through the bulk and not reaching the electrodes would still induce some signal as the Ramo weighting field will not be null even in this region.

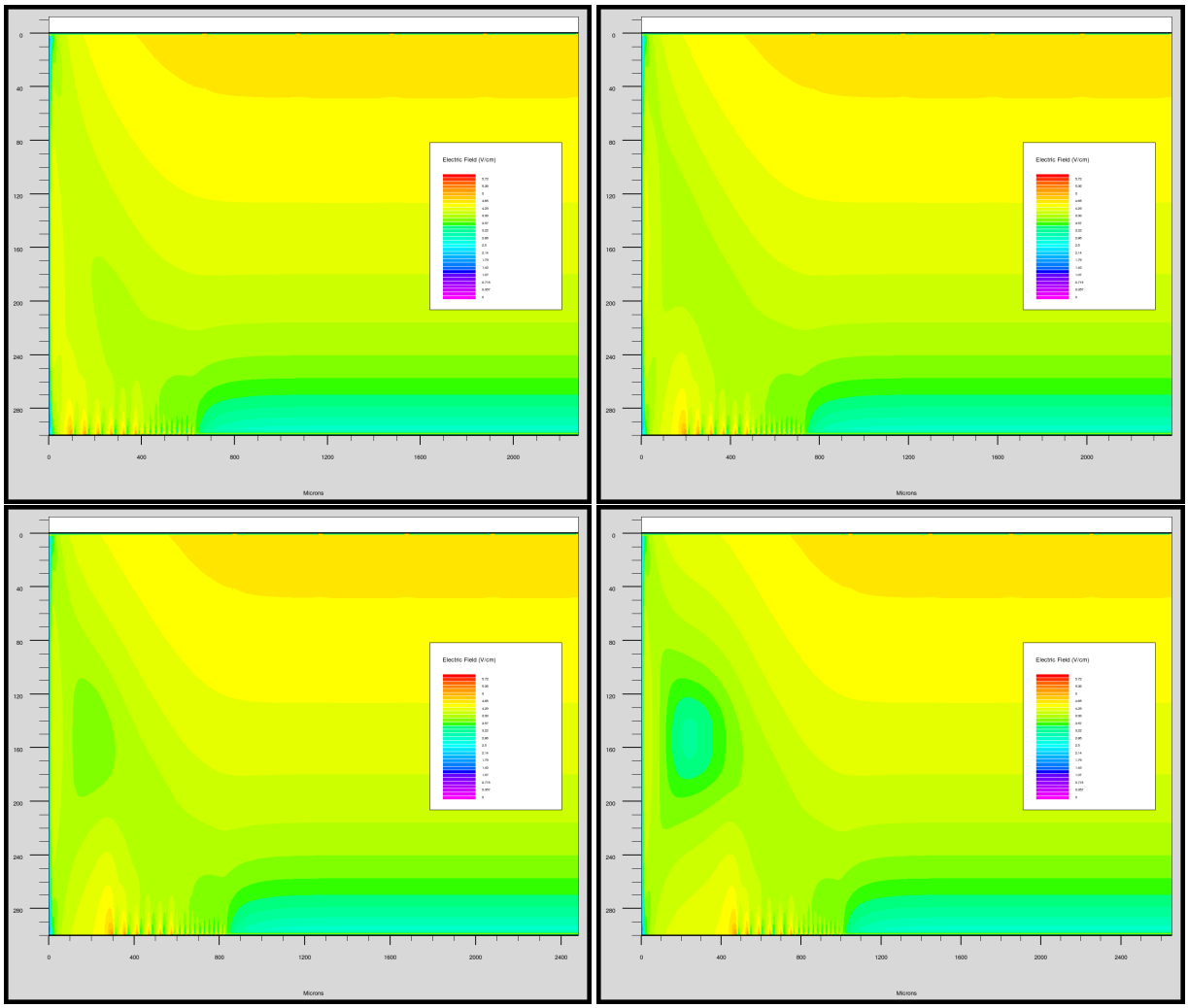

Figure 12: Simulated electric field profile for an irradiated (1e14 $n_{eq}cm^{-2}$) ATLAS pixel sensor for a dead edge width of (from left to right, top to bottom): 100, 200, 300 and 468 microns, minimum=0 maximum= 2.5e5 V/cm

6.4 Suggestion for test structures and design

The final goal of this simulation is to gain insight into the influence of the sensor design on its performance. This work aims at suggesting modifications to be done to the actual ATLAS pixel sensor design in order to increase the active surface of the sensor. Two main strategies have been explored: reducing the number of guard rings and reducing the width of the dead edge region. In section 5.2, it has been shown that with a damaged edge width of less than 100 μm, dead edge width could be safely reduced down to 100 μm. It is however unclear how lateral depletion occurs after space charge sign inversion. Comparison of the simulated results to measurements on test structures should be performed in order to constrain our model and better understand how to simulate edges after space charge sign inversion.

In Section 5.3, it has been shown that up to 4 of the outer guard rings could be removed without hurting the capacity of the guard rings to control the potential drop to the edge of the sensor. Removing 5 or more guard rings would cause the potential drop from the outermost guard ring to the edge to be too steep, generating an intense electric field that would result in breakdown of the sensor. A future work

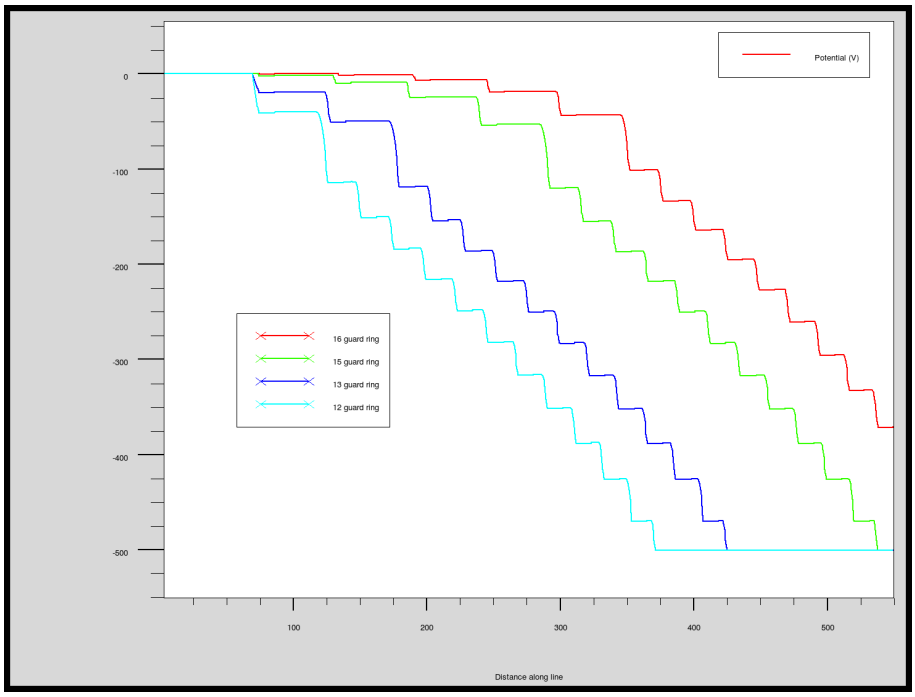

Figure 13: Simulated bias voltage distribution for actual ATLAS sensor with 0,1,3,4 of the outer guard rings removed

will aim at optimizing the guard ring width and spacing for minimizing the amount of guard rings needed for protection on normal operation of the pixel sensor.

Finally, it has been shown in this work that the behavior of the guard rings after space charge sign inversion is not well understood. Therefore, we suggest to include in a wafer production a set of test structures that would allow us to study edge behavior, fine tune our simulation and improve our models. Three structures have been proposed:

- Test structures for total and electrically active doping profiles (fig. 17)
- Contactable Multi-guard ring diodes (fig. 18)
- Baby-pixel sensors for charge sharing studies

Test structures for total and electrically active dopant study would allow us to measure doping profiles on the different implants produced in the wafer production. These profiles could be implemented in simulation in order to reproduce more accurately the electrical properties of the sensor produced. These chips will consist of simple rectangular structures of 2x14 mm with uniform implantation. A test structure would be designed for each of the implant used in the wafer production.

A set of simple diode with simple guard ring structure, consisting of 1 to 4 large guard rings, could be useful to compare guard ring behavior to simulation and fine tune parameters like oxide charge or impact ionization model parameters. This geometry would be simple to simulate and would allow us to constraint free parameters of the simulations while avoiding simplification and approximation inherent to simulation of large scale structure.

Finally, a set of small pixel sensors could be useful to study charge charing behavior of the produced sensors. Charge sharing could inform us on inter-pixel isolation and on the electric field distribution

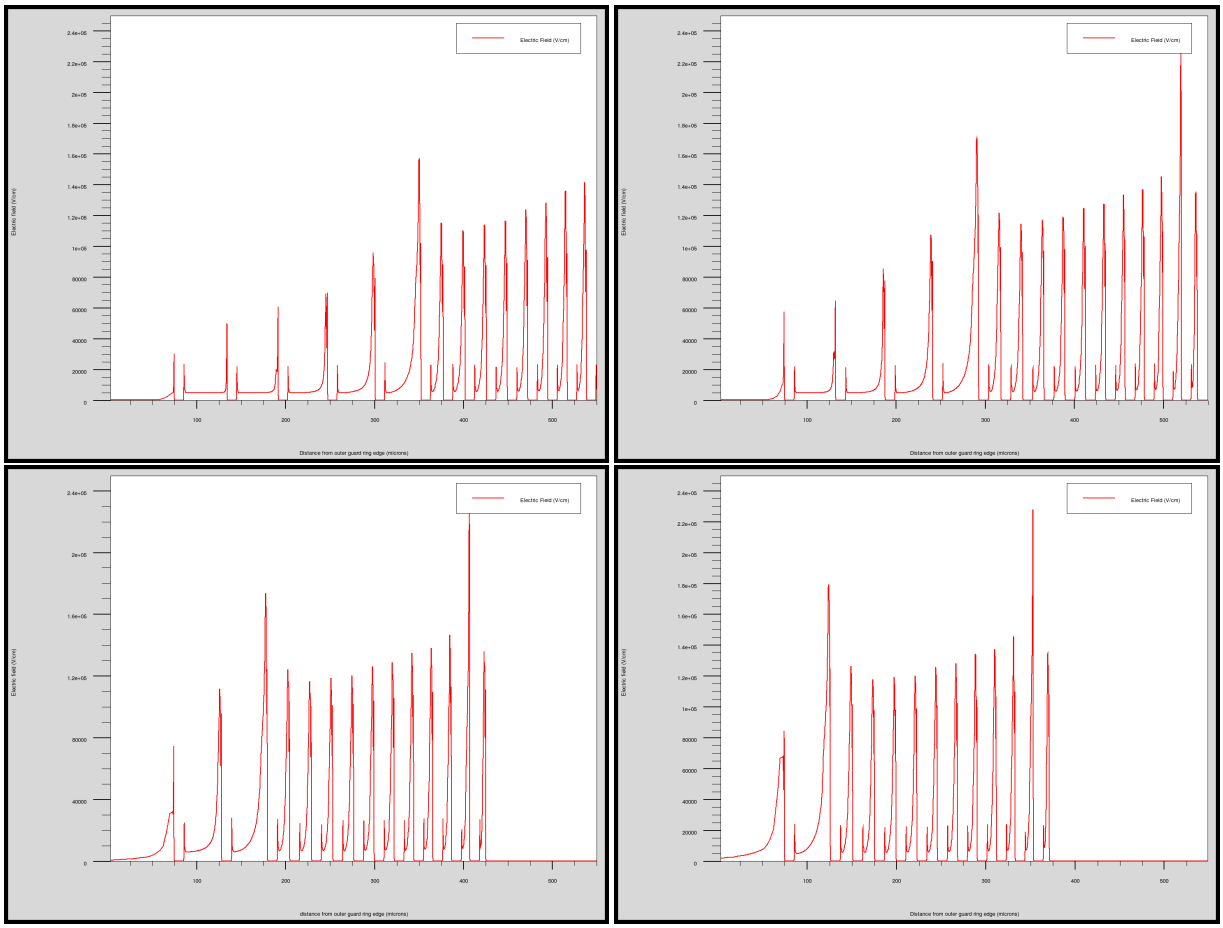

Figure 14: Simulated electric field distribution, 0.1 μm under surface, for actual ATLAS sensor with 0,1,3,4 of the outer guard rings removed, minimum=0 maximum= 2.5e5 V/cm

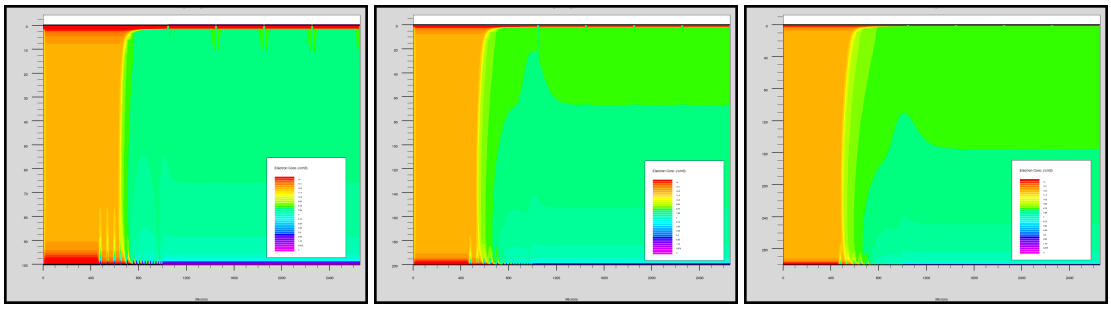

Figure 15: Electron concentration for different ATLAS pixel sensor thickness, from left to right : 100, 200, 300 μm, minimum=0 maximum =1e14 cm^{-3}

inside the sensor. Comparison of the experimental data after irradiation to simulation could be useful to constraint our models of radiation damage and our breakdown model. Finally this structure could allow us to gain information on trapping in irradiated device, which could then be simulated.

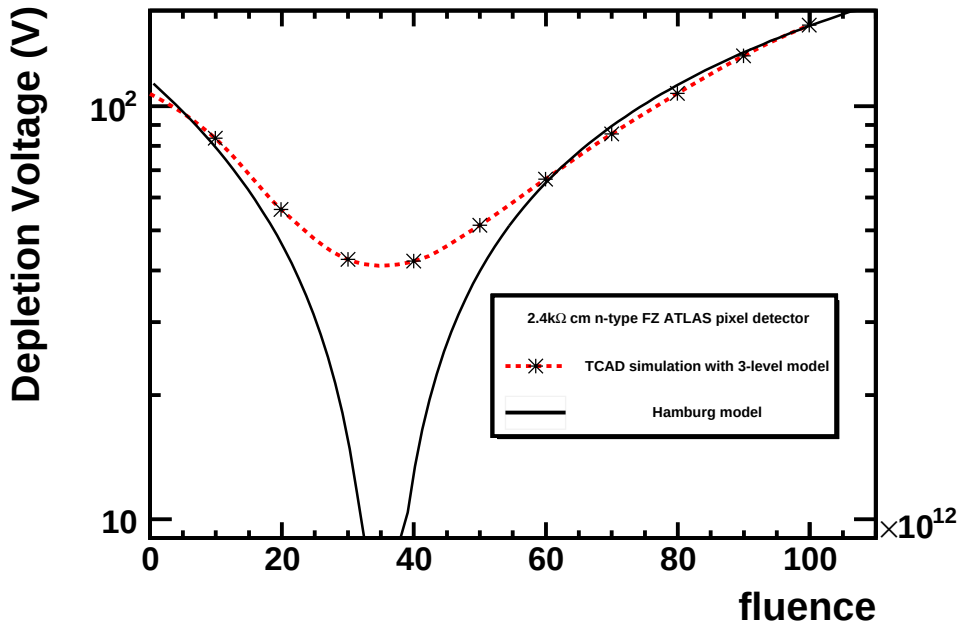

Figure 16: Space charge sign inversion in a 2.4 $k\Omega cm$ n-type ATLAS sensor, calculated from CV method with TCAD simulation data

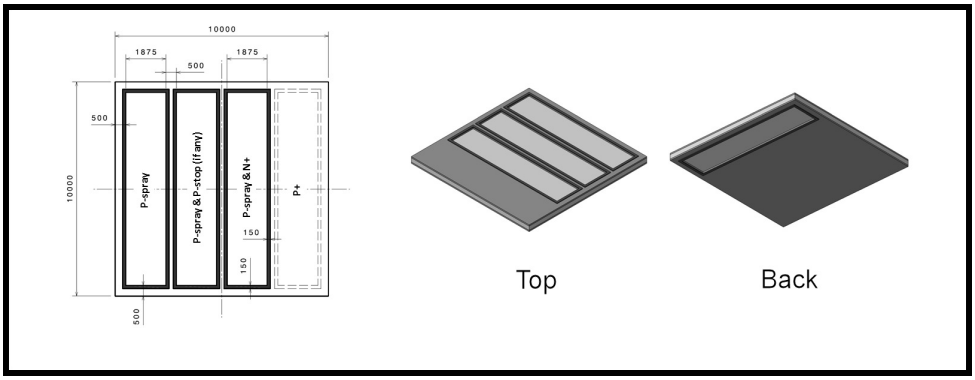

Figure 17: Test structure design for total and electrically active doping profile measurement

7 Summary and conclusion

In this work, we presented a framework to study the electrical properties of semiconductor pixel devices and simulate the actual ATLAS pixel sensors, including possible modification to their design. We performed a series of simulations with modified guard ring structure, edge width and depth, for different amounts of exposition to radiation. From the results of the simulation, we obtained two recommendations on the design : reducing the dead edge to 100 μm and removing up to 4 of the outer guard rings. We have shown that thinning can be beneficial to lower the bias voltage, leakage current and keep good signal after irradiation.

A lot of parameters need to be constrained so as to obtain more accurate simulations and to under-

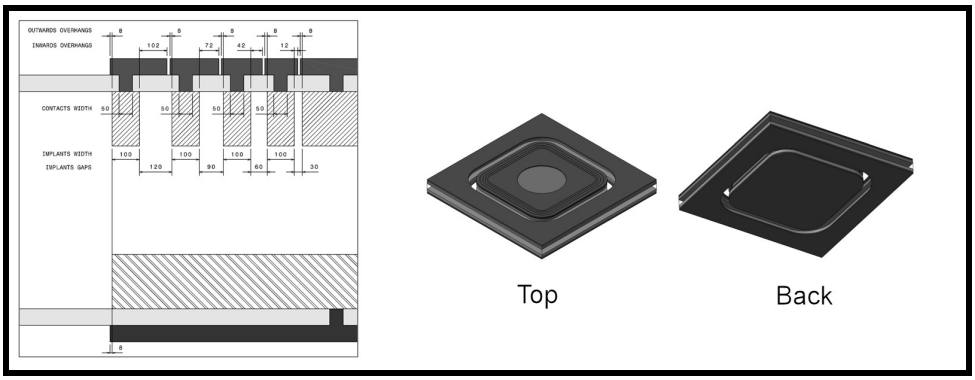

Figure 18: Contactable multi-guard rings diode design

stand better the radiation damage and guard rings behavior. We suggested a set of test structures that will help us to calibrate our simulations and improve the radiation damage model. Extensive characterization of the produced sensors coupled to simulation will allow us to do a calibration of our simulation and improve the quality of the future ATLAS tracker pixel sensors.

8 Acknowledgments

The authors would like to thank the P2I organism, Guy Wormser, Daniel Fournier and the rest of LAL ATLAS group for the financial support and the hospitality that made this work possible. A special thanks to the members of the Planar Pixel Upgrade group for their input and the discussion that allowed this work to be done.

References

[1] Ian Dawson, IBL General meeting, June 25 (2009).

[2] Hartmut F.-W. Sadrozinski and Abraham Seiden, Nucl. Instrum. Meth. A **541** (2005) 434 – 440.

[3] Yu Y. Peter and M. Cardona, Fundamentals of Semiconductors, 3rd Edition, (Springer, 2003).

[4] Moscatelli, F. and al., Nucl. Instrum. Meth. B **186** (2002) 171–175.

[5] Moscatelli, F. and al., IEEE Trans. Nucl. Sci. **51** (2004) 1759–1765.

[6] A. Ruzin, Nucl. Instrum. Meth. A **447** (2000) 116 – 125.

[7] G. Lindstrom and al., Nucl. Instrum. Meth. A **466** (2001) 308 – 326.

[8] M. Bruzzi and M. Moll, CERN RD50 Status Report 2002/2003 RD50: Radiation hard semiconductor devices for very high luminosity colliders (2003).

[9] F. Campabadal. and M. Bruzzi and M. Moll, CERN RD50 Status Report 2004: Radiation hard semiconductor devices for very high luminosity colliders (2005).

[10] M. Bruzzi and M. Moll, CERN RD50 Status Report 2005: Radiation hard semiconductor devices for very high Luminosity colliders (2005).

[11] Li, Zheng and Kraner, H., J. Electronic Materials **21** (1992) 701–705.

[12] Eremin, V. and Li, Z. and Ilyashenko, I., Nucl. Instrum. Meth. A **A360** (1995) 458–462.

[13] Menichelli, D. and Bruzzi, M. and Li, Z. and Eremin, V., Nucl. Instrum. Meth. A **426** (1999) 135–139.

[14] Siegfried Selberherr, Analysis and simulation of semiconductor devices, (Wien, 1984).

[15] M. Moll, Radiation Damage in Silicon Particle Detectors, Ph.D. thesis, University of Hamburg, 1999.

[16] Li, Z. and Huang, W. and Zhao, L. J., IEEE Trans. Nucl. Sci. **47** (2000) 729–736.

[17] Alam. and al., ATLAS Tech. design report (1998).

[18] L. Rossi and P. Fischer and T. Rohe and N. Wermes, Pixel Detectors : From Fundamentals to Applications, (Springer, 2006).

[19] Noschis, E. and Eremin, V. and Ruggiero, G., Nucl. Instrum. Meth. A **574** (2007) 420–424.

[20] SILVACO International inc., 4701 Patrick Henry Drive, bldg 1, Santa Clara, CA 95054, ATLAS User's Manual, Device Simulation Software, June 2008, V 5.14.0.R.